ELSEVIER

Contents lists available at ScienceDirect

Computational Materials Science

journal homepage: www.elsevier.com/locate/commatsci



Full Length Article



A phase-field model for interactive evolution of phase transformation and cracking in superelastic shape memory ceramics

Amirreza Lotfolahpour, William Huber, Mohsen Asle Zaeem

Department of Mechanical Engineering, Colorado School of Mines, Golden, CO 80401, USA

ARTICLE INFO

Keywords:
Phase-field model
Shape memory ceramics
Phase transformation
Fracture
Superelastic

ABSTRACT

This work presents a modified phase-field model for accurate coupling of phase transformation and cracking in shape memory ceramics. The existing phase-field models underestimate the elastic response at the beginning of the mechanical response. We modified the chemical free energy to control the rate of phase transformation and consequently obtain a physical elastic response before initiation of phase transformation. First, the forward and reverse martensitic phase transformation in a superelastic single crystal 3 mol% yttria-stabilized tetragonal zirconia is studied. Then, the interaction between phase transformation and fracture under displacement-controlled loading condition is investigated. The model predicts a realistic mechanical response and the experimentally observed microstructure and crack deflection due to the phase transformation. In addition, the model captures the reverse phase transformation and the stress drop due to the crack propagation.

1. Introduction

Shape memory ceramics (SMCs) have various applications in the biomedical and aerospace industries [1]. One of the main characteristics of SMCs is their recoverable stress/temperature-induced solid-state martensitic phase transformation (MPT), which results in strain recovery. Based on the temperature of the material, two different behaviors can be observed: superelasticity (SE) (also known as pseudoelasticity) or the shape memory effect (SME) (also known as pseudoplasticity). If the temperature is higher than the equilibrium transformation temperature, SE is observed. In SE behavior, the strain is fully recovered when the load is removed, and a stress-strain hysteresis loop is obtained [2–4]. If the temperature is lower than the equilibrium transformation temperature, the SME is observed. In SME, after removing the load there is a large residual strain and a temperature higher than the equilibrium temperature is required to recover the original shape and phase of the material [2–6].

The main ingredient of SMCs is often zirconia. Zirconia-based ceramics have high strength, high operating temperature, and high corrosion resistance which make these ceramics suitable for extreme operating conditions. In addition, they show promising SME and SE behaviors due to stress or temperature induced recoverable phase transformation between their tetragonal (T) and monoclinic (M) phases (T \leftrightarrow M). However, because these phases are brittle, zirconia-based

ceramics have a low fracture toughness. In addition, $T \to M$ phase transformation causes inelastic dilatation, which contributes to low SME and SE fatigue life in SMCs [7].

Since the overall mechanical properties and fracture behavior of materials is strongly affected by their microstructure, studying microstructure evolution and fracture at the microscopic length scale is essential to obtain an accurate estimate of durability of structures. There are a few experimental works on zirconia ceramics to study the microstructural evolution [8,9] and interaction between crack and phase transformation [10] in order to study and improve the fracture and overall mechanical properties of SMCs. In addition to requiring a considerable amount of materials, testing time and cost, experiments are unable to fully capture the interactions between cracking and phase transformation in ceramics, because both happen at a very high pace. Therefore, numerical studies could be suitable alternatives to study such interactions.

Phase-field (PF) modeling stands out as a powerful numerical approach for simulating MPT [2]. In the PF approach, the product of a phase transformation is represented by a scalar called an order parameter (OP). In addition, the PF approach has been widely applied as a powerful and robust approach for modeling fracture in brittle [11–14] and ductile materials [15,16] where an OP represents the crack surface.

Based on experimental observations, when phase transformation occurs in shape memory materials, the strain localization produces a

E-mail address: zaeem@mines.edu (M. Asle Zaeem).

^{*} Corresponding author.

twinned-martensite (strip-like microstructure) microstructure of alternating austinite-martensite or martensite-martensite variants [17,18]. To obtain a reliable mechanical response and experimentally observed microstructures, one must choose an appropriate chemical free energy in the total free energy functional of the PF model of MPT. The chemical free energy represents the energy dissipation due to MPT, and 2-3-4 and 2-4-6 polynomials are commonly used in the literature for first order transformations [2]. Depending on the parameters of the polynomial, the shape of chemical free energy can be either double-well, concave, or convex. In addition to the chemical free energy, the relationship between the OPs and the stress-free strain tensor (or OP-strain relation) plays an important role in prediction of the mechanical response.

Mamivand et al. [19] were the first to develop a PF model for $T \rightarrow M$ phase transformation in single crystal zirconia under stress-controlled loading conditions. They used a 2-4-6 polynomial and a quadratic OPstrain relation. They validated their simulated microstructure against experimental results. In another work, Mamivand et al. [20] used a similar model and studied both SE and SME in a polycrystalline zirconia under a stress-controlled loading condition; they showed that the obtained twinned-martensite microstructure and mechanical response were consistent with experiments. Recently, Cisse and Asle Zaeem [3] developed a non-isothermal elastoplastic PF model considering 2-4-6 and a quadratic OP-strain relation to study the SE and SME in both single crystal and polycrystalline 3 mol% yttria-stabilized tetragonal zirconia (3Y-STZ) under stress-controlled loading conditions. In [21], the authors used a 2-3-4 polynomial and a linear OP-strain relationship to study the ferroelastic domain switching in a zirconia crystal in the presence of crack propagation which was qualitatively compared to experimental observations. A combination of the linear OP-strain relation with 2-3-4 or 2-4-6 polynomials has also been used for modeling MPT in other shape memory materials like NiTi [22-26].

Based on the aforementioned research works, linear or quadratic OP-strain relation has been used in PF models for simulating the MPT in SMCs and shape memory alloys. We will discuss and compare linear and quadratic OP-strain relations in Sec. 2.5.1 and explain that under some circumstances the quadratic OP-strain relation loses its generality and validity. Therefore, we use the linear OP-strain relation in this paper. It is also important note that PF models of MPT underestimate the elastic modulus in the initial part of the stress-strain response regardless of the choice of the OP-strain relation; we will also address this shortcoming of the current PF models in this work.

Only a few studies investigated the interactions of MPT and cracking in SMCs. Zhao et al. [27] studied this interaction in single crystal zirconia under a displacement controlled loading condition using the PF method. They considered a chemical free energy polynomial that simulates SME. Although they obtained a twined-martensite microstructure as a result of the SME chemical free energy polynomial, they did not report the mechanical response in the form of a stress-strain curve, and it is not expected that the employed formulations generate a reasonable mechanical response. Zhu and Lao [28] used the same PF model in [27] to study phase transformation and fracture in polycrystalline zirconia. Their work lacked prediction of the mechanical response as well.

Moshkelgosha et al. [29] studied fracture propagation in single crystal zirconia and separately in polycrystalline zirconia [30] adopting a chemical free energy polynomial that simulates SME. They applied a stress-controlled loading condition. Although they obtained experimentally observed twinned-martensite microstructures, their mechanical response did show any drop in the stress-strain curve when a crack initiated and propagated. Also, they predicted a maximum strain of at least 5.5% for a single crystal and 12% for a polycrystal before fracture fully developed, which is unphysical. This is an indication that stress-controlled loading is not appropriate to predict strength from a fracture simulation. In a different study by the same authors [31], they studied phase transformation and fracture in a 3D single crystal zirconia by applying a displacement-controlled loading, however, they did not show any drop in the stress-strain curve after crack initiation and

propagation. Also, their maximum reported strain under uniaxial tension was 15%, while the experimental work by Lai et al. [8] reported a maximum bending strain of 8%. Therefore, it is expected that a specimen under uniaxial tension fails at a lower strain.

Generally, since most of the experimental studies for determining the mechanical properties are under displacement-controlled loading conditions [32–40], the numerical results obtained under stress-controlled loading cannot be compared and validated with experiments. Especially, when the goal is to study crack propagation in a continuum model, quasi-static stress-controlled loading cannot be used, because when the crack propagation starts, the stress-controlled loading causes unbounded displacement and the final drop in the mechanical response cannot be obtained by the stress-controlled loading conditions [41].

Based on the above literature review, we can conclude that none of the current PF models can properly simulate the coupled phase transformation and fracture in SMCs and produce acceptable microstructures and stress–strain curves under displacement-controlled loading conditions. In this paper, first, we examine the double well, concave, and convex chemical energies, to determine which functional form produces the most accurate predictions of microstructure and mechanical response. Then, we propose a solution to the under-prediction of the elastic modulus observed in PF simulations of SE. Finally, we show that, with the proposed modification, accurate predictions of the interaction between MPT and fracture can be made using the PF approach.

2. Coupling PT and fracture in PF context

We use OPs noted as η_p to describe the state of pth monoclinic variants. The η_p varies between 0 and 1, and $\eta_p = 1$ means the pth monoclinic variant exists and when $\eta_p = 0$, the other monoclinic variants or the tetragonal phase exist. To derive the governing equations for MPT, first we need to construct the total free energy of the system (F_{tot}):

$$F_{\text{tot}}(u_i, \eta_1, \eta_2, \dots, \eta_m) = F_{\text{el}} + F_{\text{ch}} + F_{\text{gd}}, \qquad (1)$$

where $F_{\rm el}$ is elastic strain energy density, $F_{\rm ch}$ is chemical free energy, and $F_{\rm gd}$ is gradient energy of the tetragonal- monoclinic or monoclinic-monoclinic phases. In the following, each of these energies is explained in detail.

2.1. Elastic strain energy (Fel)

The elastic strain energy can be written as:

$$F_{\text{el}}(u_i) = \int_{V_2} \frac{1}{2} C_{ijkl} \mathcal{E}_{kl}^{\text{el}} \mathcal{E}_{ij}^{\text{el}} dV, \tag{2}$$

where V is the domain volume, u_i is the displacement, C_{ijkl} is the elastic tensor and ε_{ij}^{el} is the elastic strain which is defined as the difference between total strain (ε_{ii}^{tot}) and the transformation strain (ε_{ii}^{tr}):

$$\varepsilon_{ii}^{\text{el}} = \varepsilon_{ii}^{\text{tot}} - \varepsilon_{ii}^{\text{tr}} \tag{3}$$

where considering the linear OP-strain relation [22,24,42], $\epsilon_{ij}^{\rm tr}$ is defined as:

$$\varepsilon_{ij}^{\rm tr} = \sum_{n=1}^{m} \varepsilon_{ij}^{00}(p) \eta_p, \tag{4}$$

where ε_{ij}^{00} is the stress-free strain tensor which represents the change in microstructure between parent and product phases [3]. It should be noted that in this paper, the small strain assumption ($\varepsilon_{ij}^{\text{tot}} = \frac{1}{2}(u_{i,j} + u_{j,i})$), is considered. We use the linear relation, and the reason is explained in Sec. 2.5.1 based on comparing the linear and quadratic OP-strain relations.

The elastic constant difference between tetragonal and monoclinic

phases is represented by the following relation [3]:

$$C_{ijkl}(\eta_1, \eta_2, \dots, \eta_m) = C_{ijkl}^{\mathrm{T}} + \sum_{p=1}^m \eta_p \left(C_{ijkl}^{\mathrm{M}} - C_{ijkl}^{\mathrm{T}} \right), \tag{5}$$

where $C_{ijkl}^{\rm T}$ and $C_{ijkl}^{\rm M}$ are elastic constants of the tetragonal and monoclinic phases, respectively. The elastic energy defined in Eq. (2) is based on Hooke's law and thus, the stress tensor is related to elastic strain tensor through the following equation:

$$\sigma_{ij}(u_i) = C_{ijkl}(\eta_1, \, \eta_2, \cdots, \, \eta_m) \varepsilon_{kl}^{\text{el}}, \tag{6}$$

2.2. Chemical free energy (F_{ch})

The $F_{\rm ch}$ drives the MPT and the shape of this energy plays an important role in predicting the mechanical response and microstructure. The 2-3-4 or 2-4-6 Landau polynomials defined in terms of OPs are the most common types of $F_{\rm ch}$ used in the literature. Wen et al. [43] explained that the particular order of the Landau polynomial does not have a significant effect on the predicted microstructure. Therefore, we use the 2-3-4 Landau polynomial:

$$F_{\rm ch}(\eta_1, \ \eta_2, ..., \ \eta_m) = \int_V \Delta G\left(a \sum_{p=1}^m \eta_p^2 - b \sum_{p=1}^m \eta_p^3 + c \left(\sum_{p=1}^m \eta_p^2\right)^2\right) dV, \quad (7)$$

where ΔG is the chemical driving force which is the difference in the specific $F_{\rm ch}$ between the parent and the product phases. According to [3,44], the following equation can be used to calculate ΔG for 3Y-STZ at different temperatures:

$$\Delta G(t \to m) = -6159.18 + 6.98T, \tag{8}$$

where the energy is in $\mathrm{Jmol}^{-1}(\mathrm{or}\ \mathrm{Jm}^{-3})$ and the temperature (T) is in Kelvin (K).

In Eq. (7) a, b, and c are coefficients that should be chosen in a way that maintains the value of the interfacial energy within the physical reasonable range and yields $F_{\rm ch} = \Delta G(t \rightarrow m)$ at $\eta_p = 1$. In addition, the values of these parameters determine the shape of $F_{\rm ch}$. Although a variety of shapes can be obtained through tuning expansion coefficients, the double-well, concave, convex have been used in the literature for modeling SE behavior. In Sec.3.1, we will study the difference between these three types of $F_{\rm ch}$ in terms of mechanical response and microstructure for modeling SE behavior in a single crystal 3Y-STZ sample.

2.3. Gradient free energy

Gradient free energy represents the interfacial energy between tetragonal-monoclinic or monoclinic-monoclinic phases and ensures a

$$F_{\rm gd}(\eta_1, \eta_2, ..., \eta_m) = \int_{V^2} \frac{\beta}{2} \sum_{p=1}^m (\nabla \eta_p)^2 dV.$$
 (10)

2.4. Coupling MPT with fracture

We use ϕ as the OP of fracture, and when $\phi=1$ the crack is fully developed and when $\phi=0$ the material is undamaged. In order to couple MPT with PF fracture, we modify the total free energy of the system by adding the fracture energy ($F_{\rm fr}$) and degrading the elastic constants based on the evolution of fracture through multiplying it by a degradation function, $g(\phi)$. These modifications lead to:

$$F_{\text{tot}}(u_i, \eta_1, \eta_2, \dots, \eta_m, \phi) = F_{\text{el}} + F_{\text{ch}} + F_{\text{gd}} + F_{\text{fr}},$$
 (11)

where $F_{\rm fr}$ is defined as [45]:

$$F_{\rm fr}(\phi) = \int_{V} G_{c} \left(\frac{\phi^{2}}{2k} + \frac{k}{2} |\nabla \phi|^{2}\right) dV, \tag{12}$$

where G_c is the fracture surface energy in Griffith's theory, and k is a positive regularization parameter with the dimension of length to regulate the width of the crack phase field.

In addition, to accommodate the crack phase field, $F_{\rm el}$ is redefined as:

$$F_{\text{el}}(u_i, \phi) = \int_{V^2} \frac{1}{2} g(\phi) C_{ijkl}(\eta_1, \ \eta_2, ..., \ \eta_m) \varepsilon_{kl}^{\text{el}} \varepsilon_{ij}^{\text{el}} dV, \tag{13}$$

where $g(\phi)$ is the degradation function and $g(\phi) = (1 - \phi)^2$ is one of the widely used degradation functions [46,47] that we use in this paper as well. Also, based on Eq. (13), the stress tensor (Eq. (6)) will change to:

$$\sigma_{ii}(u_i, \phi) = g(\phi) C_{iikl}(\eta_1, \eta_2, \dots, \eta_m) \varepsilon_{kl}^{el}. \tag{14}$$

In this paper, we use the method proposed by Miehe et al. [48] to ensure irreversibility of crack (crack healing prevention):

$$F_{el}(u_i, t) = \max F_{el}(u_i, s), s \in [0, t].$$
(15)

2.5. Governing equations

The evolution of both MPT and PF fracture can be obtained through Ginzburg-Landau equation [49,50]. This equation relates the rate of each OP to the variational derivative of total free energy with respect to the same OP. Using Ginzburg-Landau equation for MPT leads to the following equation:

$$\frac{\partial \eta_p}{\partial t} = -L\left(\frac{\delta F_{\text{tot}}}{\delta \eta_p}\right) = -L\left(\frac{\delta F_{\text{el}}}{\delta \eta_p} + \frac{\delta F_{\text{ch}}}{\delta \eta_p} + \frac{\delta F_{\text{gd}}}{\delta \eta_p} + \frac{\delta F_{\text{fr}}}{\delta \eta_p}\right),\tag{16}$$

where L is the kinetic coefficient, and:

$$\frac{\delta F_{\text{el}}}{\delta \eta_{\text{o}}} = \frac{1}{2} g(\phi) \varepsilon_{ij}^{\text{el}} \left(C_{ijkl}^{\text{M}} - C_{ijkl}^{\text{T}} \right) \varepsilon_{kl}^{\text{el}} - \frac{1}{2} g(\phi) C_{ijkl}(\eta_1, \eta_2, \dots, \eta_m) \varepsilon_{kl}^{00}(p) \varepsilon_{ij}^{\text{el}} - \frac{1}{2} g(\phi) C_{ijkl}(\eta_1, \eta_2, \dots, \eta_m) \varepsilon_{ij}^{00}(p) \varepsilon_{kl}^{\text{el}}, \tag{17}$$

non-abrupt transition between different phases. It is defined as:

$$F_{\rm gd}(\eta_1, \eta_2, ..., \eta_m) = \int_{V} \frac{\beta_{ij}}{2} \sum_{p=1}^{m} \nabla_i \eta_p \nabla_j \eta_p dV,$$
 (9)

where ∇ is the gradient operator and β_{ij} is gradient energy tensor. We assume that the gradient energy coefficient is isotropic ($\beta_{ij} = \beta \delta_{ij}$) [3]. Therefore the Eq. (9) will be:

$$\frac{\delta F_{\rm ch}}{\delta \eta_p} = \Delta G \left(2a\eta_p - 3b\eta_p^2 + 4c\eta_p \sum_{p=1}^m \eta_p^2 \right),\tag{18}$$

$$\frac{\delta F_{\rm gd}}{\delta \eta_p} = -\beta \nabla^2 \eta_p,\tag{19}$$

$$\frac{\delta F_{\rm fr}}{\delta n_n} = 0. \tag{20}$$

Also, using the Ginzburg-Landau equation for PF fracture leads to:

$$\frac{\partial \phi}{\partial t} = -M \left(\frac{\delta F_{\text{tot}}}{\delta \phi} \right) = -M \left(\frac{\delta F_{\text{el}}}{\delta \phi} + \frac{\delta F_{\text{ch}}}{\delta \phi} + \frac{\delta F_{\text{gd}}}{\delta \phi} + \frac{\delta F_{\text{fr}}}{\delta \phi} \right), \tag{21}$$

where *M* is called the fracture mobility coefficient, and:

$$\frac{\delta F_{\text{el}}}{\delta \phi} = -(1 - \phi) C_{ijkl}(\eta_1, \eta_2, \dots, \eta_m) \varepsilon_{kl}^{\text{el}} \varepsilon_{ij}^{\text{el}}, \tag{22}$$

$$\frac{\delta F_{\rm ch}}{\delta \phi} = 0,\tag{23}$$

$$\frac{\delta F_{\rm gd}}{\delta \phi} = 0, \tag{24}$$

$$\frac{\delta F_{\rm fr}}{\delta \phi} = G_c \left(\frac{\phi}{k} - k \nabla^2 \phi \right). \tag{25}$$

Examination of Eq. (3) and Eq. (17) reveals that MPT can have a blunting effect on the crack initiation and propagation through reducing the available elastic energy. Meanwhile, based on Eq. (22), fracture halts the propagation of MPT by reducing elastic strain energy in the cracked regions ($\phi > 0$).

In addition, by neglecting the body forces, the equilibrium equations become:

$$\operatorname{div} \boldsymbol{\sigma}(u_i, \phi) = 0. \tag{26}$$

2.5.1. The difference between linear and quadratic OP-strain relations

As it was mentioned before, in this paper we use the linear OP-strain relation. We chose the linear relation over the quadratic relation because the quadratic relation can become invalid in some situations explained below.

Using the linear relation, the OPs' evolution equation (Eq. (16)) without considering the effect of fracture, will become:

$$\begin{split} \frac{\partial \eta_{p}}{\partial t} &= -L \left(\frac{1}{2} \varepsilon_{ij}^{\text{el}} \left(C_{ijkl}^{\text{M}} - C_{ijkl}^{\text{T}} \right) \varepsilon_{kl}^{\text{el}} - \frac{1}{2} C_{ijkl} (\eta_{1}, \eta_{2}, \dots, \eta_{m}) \varepsilon_{kl}^{00}(p) \varepsilon_{ij}^{\text{el}} \right. \\ &\left. - \frac{1}{2} C_{ijkl} (\eta_{1}, \eta_{2}, \dots, \eta_{m}) \varepsilon_{ij}^{00}(p) \varepsilon_{kl}^{\text{el}} + \Delta G \left(2a \eta_{p} - 3b \eta_{p}^{2} + 4c \eta_{p} \sum_{p=1}^{m} \eta_{p}^{2} \right) \right. \\ &\left. - \beta \nabla^{2} \eta_{p} \right). \end{split} \tag{27}$$

The quadratic relation $(\varepsilon_{ij}^{\rm tr}=\sum_{p=1}^m \varepsilon_{ij}^{00}(p)\eta_p^2)$ leads to the following equation for the OPs' evolution:

$$\begin{split} \frac{\partial \eta_p}{\partial t} &= -L \Biggl(\frac{1}{2} \varepsilon_{ij}^{\text{el}} \Biggl(C_{ijkl}^{\text{M}} - C_{ijkl}^{\text{T}} \Biggr) \varepsilon_{kl}^{\text{el}} - \eta_p C_{ijkl} (\eta_1, \eta_2, \cdots, \eta_m) \varepsilon_{kl}^{00}(p) \varepsilon_{ij}^{\text{el}} \\ &- \eta_p C_{ijkl} (\eta_1, \eta_2, \cdots, \eta_m) \varepsilon_{ij}^{00}(p) \varepsilon_{kl}^{\text{el}} + \Delta G \Biggl(2a \eta_p - 3b \eta_p^2 + 4c \eta_p \sum_{p=1}^m \eta_p^2 \Biggr) \\ &- \beta \nabla^2 \eta_p \Biggr). \end{split}$$

$$(28)$$

In Eq. (28), all terms except the first term are zero when the initial value of $\eta_p=0$. Then if $\left(C_{ijkl}^{\rm M}-C_{ijkl}^{\rm T}\right)$ is zero (e.g. if MPT in polycrystalline samples [22] or if ferroelastic domain switching [21] is studied) Eq. (28) becomes zero and consequently η_p never grows. Therefore, Eq. (28) loses its generality and validity and cannot accurately predict MPT. This problem does not occur when the linear OP-strain relation is considered since the second term in Eq. (27) is not zero and starts to increase upon the start of loading and never loses its generality and validity. Therefore, we use the linear OP-strain relation in this paper.

2.6. Solution scheme

The governing equations presented in the previous section are solved in a finite element framework using the solid mechanics and mathematics modulus of COMSOL multiphysics. All simulations are under displacement-controlled loading, and the boundary conditions and sample dimensions are shown in Fig. 1a. Also, Fig. 1b shows the applied

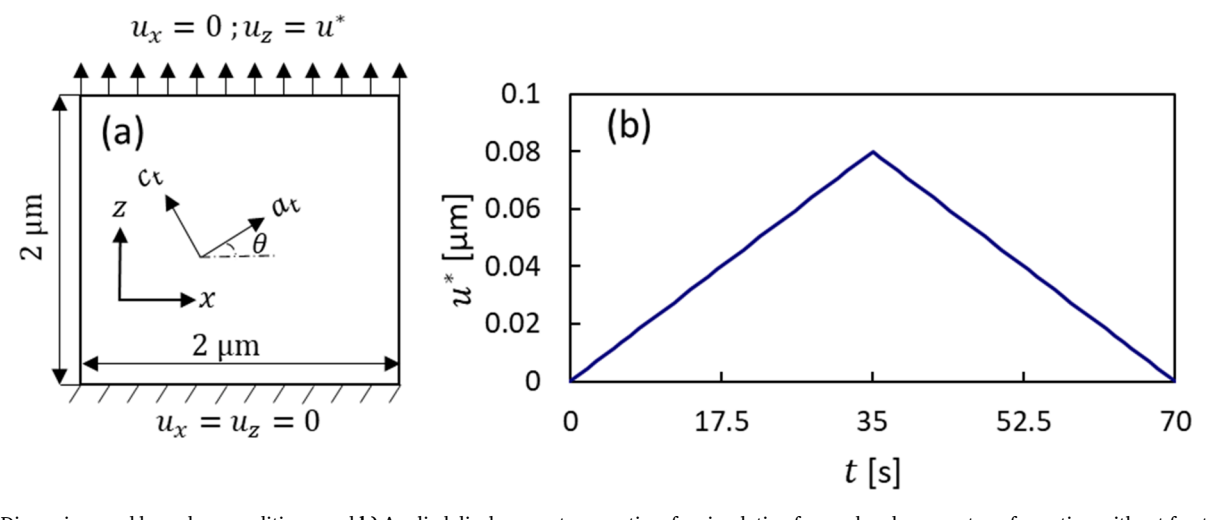


Fig. 1. a) Dimensions and boundary conditions, and b) Applied displacement versus time for simulating forward and reverse transformation without fracture. x- axis represents a_t direction and z axis represent c_t of the tetragonal phase.

Table 1Coefficients of different chemical free energies.

Coefficient	Double-Well	Concave	Convex
а	13.89	9.2	3.13
b	23.75	12.89	4.01
c	10.78	4.74	1.85

displacement versus time. Furthermore, the plane stress condition is considered in all 2D simulations.

For all models, with and without fracture, quadrilateral elements are generated by the mapped mesh algorithm feature in COMSOL. A mesh study was conducted where we found that a mesh size of 0.04 μm (or 2500 quadrilateral elements in the domain) were sufficient to resolve the interface of different phases. Discretizing the sample with more elements did not change the microstructure and mechanical response, therefore we used 2500 quadrilateral elements. The displacements are solved using "Solid Mechanics" module with quadratic shape functions. The crack PF and Martensite PF are solved using the "General Form PDE" module of COMSOL with linear shape functions. The staggered [51] scheme is used to solve the governing equations where nonlinear sub-problems are solved with Newton's method. The time step of 0.01 s is used for all simulations.

3. Results and discussions

3.1. Comparison of different F_{ch} for modeling SE in 3Y-STZ

In this section, we compare three different forms of $F_{\rm ch}$ (double-well, concave and convex) for modeling SE in a 2D idealization of a 3Y-STZ single crystal sample without considering fracture. Table 1 shows the values of a, b, and c for each $F_{\rm ch}$. These parameters are determined to ensure each $F_{\rm ch}$ has a minimum at $\eta=0$. For the double-well case, the energy has a local minimum at $\eta=1$ as well. Also in all three $F_{\rm ch}$, ΔG (in Eq. (7)) is $\sim 156~{\rm Jmol}^{-1}~(7.2\times 10^6~{\rm Jm}^{-3})$ which is obtained by Eq. (8) considering the temperature is constant at 905K. This temperature is higher than the reported equilibrium temperature of 883 K for 3Y-STZ [3,52,53], therefore, the system will show SE behavior (i.e., strain recovery occurs after unloading without a need for increasing the temperature). Fig. 2 shows the plot of these three forms of $F_{\rm ch}$.

Eq. (29) and Eq. (30) show the stiffness tensor of tetragonal [54,55] and monoclinic [55], respectively. In addition, two monoclinic variants exist in the a-c plane, and their stress-free strain tensors are given in Eq. (31) and Eq. (32) [19].

$$\boldsymbol{C}_{ijkl}^{T} = \begin{bmatrix} 361 & 100 & 62 & 0 & 0 & 0 \\ 100 & 361 & 62 & 0 & 0 & 0 \\ 62 & 62 & 264 & 0 & 0 & 0 \\ 0 & 0 & 0 & 59 & 0 & 0 \\ 0 & 0 & 0 & 0 & 59 & 0 \\ 0 & 0 & 0 & 0 & 0 & 64 \end{bmatrix} GPa,$$
(29)

$$C_{ijkl}^{M} = \begin{bmatrix} 327 & 142 & 55 & 0 & 0 & -21 \\ 142 & 408 & 196 & 0 & 0 & 31 \\ 55 & 196 & 258 & 0 & 0 & -18 \\ 0 & 0 & 0 & 100 & -23 & 0 \\ 0 & 0 & 0 & -23 & 81 & 0 \\ -21 & 31 & -18 & 0 & 0 & 126 \end{bmatrix} GPa,$$
(30)

$$\varepsilon_{ij}^{00}(1) = \begin{bmatrix} 0.0049 & -0.0761 \\ -0.0761 & 0.0180 \end{bmatrix}, \tag{31}$$

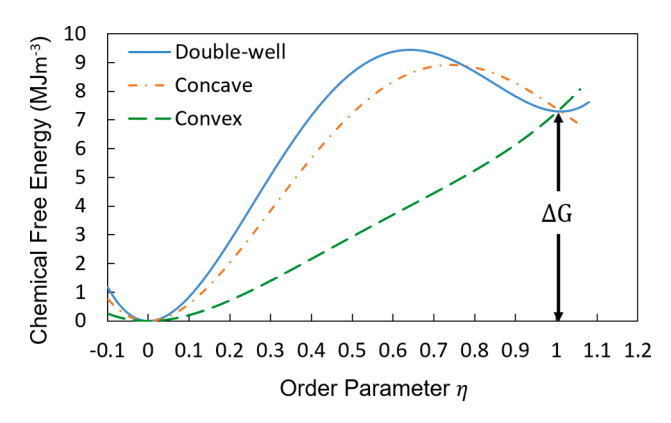


Fig. 2. Three different $F_{\rm ch}$ used for modeling SE.

$$\varepsilon_{ij}^{00}(2) = \begin{bmatrix} 0.0049 & 0.0761\\ 0.0761 & 0.0180 \end{bmatrix}. \tag{32}$$

We consider the global coordinates when $\theta=0^\circ$, to be aligned with those of the tetragonal phase where x- axis represents a_t direction and z axis represents c_t (see Fig. 1a) and $\theta=0^\circ$ corresponds to [001] oriented crystal. The stress-free strain tensor and elastic stiffness tensor are transferred to the global coordinate system using the following rotation operations:

$$\varepsilon_{ij}^{000}(p) = R_{ik}R_{jl}\varepsilon_{kl}^{00}(p), \tag{33}$$

$$C_{iikl}^G = R_{im}R_{jn}R_{ko}R_{lp}C_{mnop}, (34)$$

where $\varepsilon_{ij}^{00}(p)$ and C_{mnop} are, respectively, the stress-free strain tensor and the elastic stiffness matrix in the local coordinate system. R_{ij} is the rotation matrix for a grain with an orientation angle of θ , which in 2D is defined as:

$$R_{ij} = \begin{bmatrix} \cos(\theta) & \sin(\theta) \\ -\sin(\theta) & \cos(\theta) \end{bmatrix}. \tag{35}$$

 θ measures positive counterclockwise. Table 2 shows all other parameters used for running the simulations. It is worth mentioning, the kinetic coefficient (L) in Eq. (16) can be arbitrary selected since there is not a report on the speed of PT in zirconia-based ceramics [20] and a wide range value from $2\times 10^{-9\frac{m^3}{J_8}}$ [29–31] to $10\frac{m^3}{J_8}$ [3] has been used in the literature. In this paper we choose this value to be $5\times 10^{-8\frac{m^3}{J_8}}$. The gradient energy coefficient (β) in Eq. (19) must be selected such that gives a reasonable interface thickness (few nanometers) [20,56], we chose $\beta=1\times 10^{-9}$ $\frac{1}{m}$ and based on the our results gives a reasonable interface thickness between different phases. Furthermore, the initial values of η_p are set to 10^{-6} to overcome the possibility of numerical artifacts. In addition, considering the crack length scale parameter (k) in Eq. (12) to be 20nm which is one percent of the domain length, is small enough to obtain a stable solution, a correct crack path, and an admissible diffusive area with a reasonable accuracy and computing cost

Table 2 Simulation parameters.

Parameter	Value
Kinetic coefficient, L	$5 \times 10^{-8} \frac{m^3}{I_s}$
Gradient energy coefficient, eta	$1 \times 10^{-9} \frac{J}{m}$
Mobility coefficient, M [57,58]	$1\frac{m^3}{Js}$
Critical energy release rate, G_c [60]	$24\frac{J}{m^2}$
Crack length scale parameter, k	20 nm

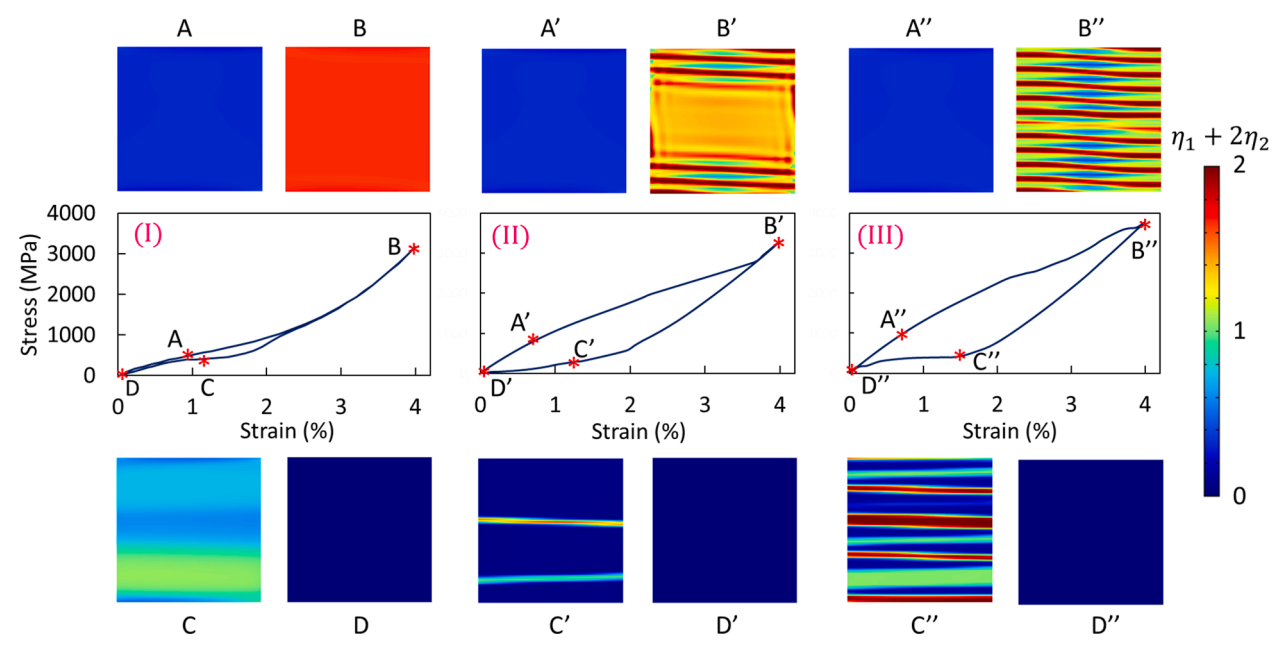


Fig. 3. Predicted stress-strain curve and microstructure for [001] orinted smaple by (I) Convex, (II) Concave, and (III) Double-well Fch.

[57-59].

Fig. 3 (I), (II), and (III) show the mechanical response and microstructure for [001] oriented sample predicted by convex, concave, and double-well $F_{\rm ch}$, respectively. In Fig. 3, the expression of $\eta_1 + 2\eta_2$ is used to show the transformed regions, and if this expression is equal to 0, no transformation has occurred and the tetragonal phase exists, if this expression is 1, the first variant of the monoclinic phase exits, and if it is equal to 2, the second variant of the monoclinic phase exists. In addition, the stress and strain in stress-strain curve are calculated based on the reaction force and the displacement at the top edge of sample. Based on these figures both double-well and concave predict the experimentally observed twinned-martensite microstructure. However, the convex F_{ch} is not able to predict such a twinned-martensite microstructure, therefore it is not a proper F_{ch} for modeling microstructures of shape memory materials. There are several works, such the MPT model used by Simoes and Martínez-Pañeda [4] for simulating fracture in shape memory materials, that used a convex potential energy, which are unable to properly predict microstructures in shape memory materials and are appropriate for macroscopic length scales. The microstructures predicted by the concave F_{ch} is consistent with previously reported results, such as those reported by Esfahani et al. for SE in NiTi alloys [61]. Although, both double-well and concave F_{ch} predict admissible microstructures and mechanical response, we proceed with the double-well $F_{\rm ch}$ because it grantees stability at both parent and product phases through having minima at both $\eta_p = 0$ and 1.

According to Fig. 3, although all three forms of $F_{\rm ch}$ yield a hysteresis strain-strain curve, none of them predicts a plateau region when the transformation starts, while this is observed in the experimental stress-strain curves for shape memory materials. Also, it is worth noting that the stress at each strain and the ultimate stress (the stress at the highest strain), is different in these three cases. This can be explained based on the fact that the first derivative of $F_{\rm ch}$ with respect to OPs determines the evolution rate of the OPs (Eq.(16)), and this determines the rate of the

transformation strain tensor (Eq. (4)). On the other hand, the transformation strain rate directly affects the rate of subtraction of the stress-free strain tensor from the total strain tensor, and this consequently changes the elastic strain tensor rate (Eq. (3)). Also, since the stress tensor is calculated based on the elastic strain tensor (Eq. (14)), each $F_{\rm ch}$ leads to a different stress at each strain.

The elastic modulus in the beginning of the stress-strain curve should be close to 247 GPa which is the inverse of the second diagonal component of the compliance tensor of tetragonal phase (the c_t axis of the crystal is along the z-direction). Since we use the double-well $F_{\rm ch}$, the elastic modulus based on Fig. 3(III) is calculated to be 160 GPa, which is about 35% lower than 247 GPa. This means the elastic modulus is highly affected by MPT. The same issue appears in most of previous works, regardless of the choice of the chemical free energy or OP-strain relation [23,42,62–64]. To address this issue, we propose a modification to the $F_{\rm ch}$ in the following section.

3.2. Modification of the chemical free energy (F_{ch})

In Fig. 3, all three forms of $F_{\rm ch}$ yield a hysteresis stress-strain curve, but in all three stress-strain curves a plateau region (or a region with low or even negative hardening) is missing, and most importantly the elastic modulus is underestimated in the beginning of the stress-strain curve. This problem is be rooted in the Eq. (16). This equation which expresses the evolution (the rate) of each OP, is dependent on the first derivative of the $F_{\rm ch}$ with respect to each OP (Eq. (18)). On the other hand, the rate of OPs affects the rate of the elastic strain tensor (Eq. (3)), and the rate of the elastic strain tensor affects the stress (Eq. (26)). Therefore, by controlling the first derivate of $F_{\rm ch}$ with respect to OPs, the rate of OPs and subsequently the shape of the mechanical response can be controlled. Based on the above explanation, we propose the following modification to the $F_{\rm ch}$:

$$F_{ch}(\eta_1, \ \eta_2, ..., \ \eta_m) = \int_V \Delta G \left(a \sum_{p=1}^m \eta_p^2 - b \sum_{p=1}^m \eta_p^3 + c \left(\sum_{p=1}^m \eta_p^2 \right)^2 + d \sum_{p=1}^m \left| \eta_p \right|^n \right) dV; 1 < n < 2,$$

$$(36)$$

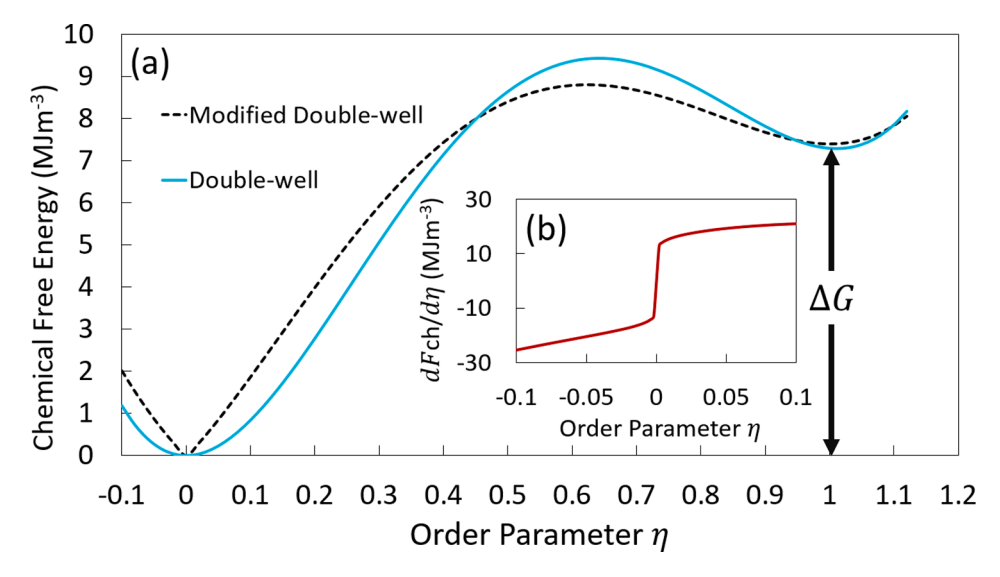


Fig. 4. a) The modified double-well versus double-well form of F_{ch} , and **b)** The first derivative of the modified double-well form of F_{ch} with respect to η around $\eta = 0$.

Table 3Coefficients of the modified chemical free energy (Eq. (36)).

nee chergy (Eq. (00)).			
а	2.64		
b	10.04		
с	5.37		
d	3.05		
n	0.1		

where d and n are new coefficients to be determined in addition to a, b, and c. Parameter n takes a value between 1 and 2, and in this paper, we consider it to be equal to 1.1. This parameter should be small enough (close to 1) to keep the elastic modulus unaffected by the OP at the beginning of loading by approximating a linear term in $F_{\rm ch}$ (Eq. (36)). To elaborate more, the added term $(d\sum_{p=1}^m |\eta_p|^n)$, at the beginning of the loading (when the OPs are small) adds a considerable amount of positive energy to the system (see Eq. (16), Eq. (36), and Eq. (37)) which slows down the evolution rate of OPs. Therefore, at the beginning of loading, the material behaves elastically. It should be noted that we use absolute

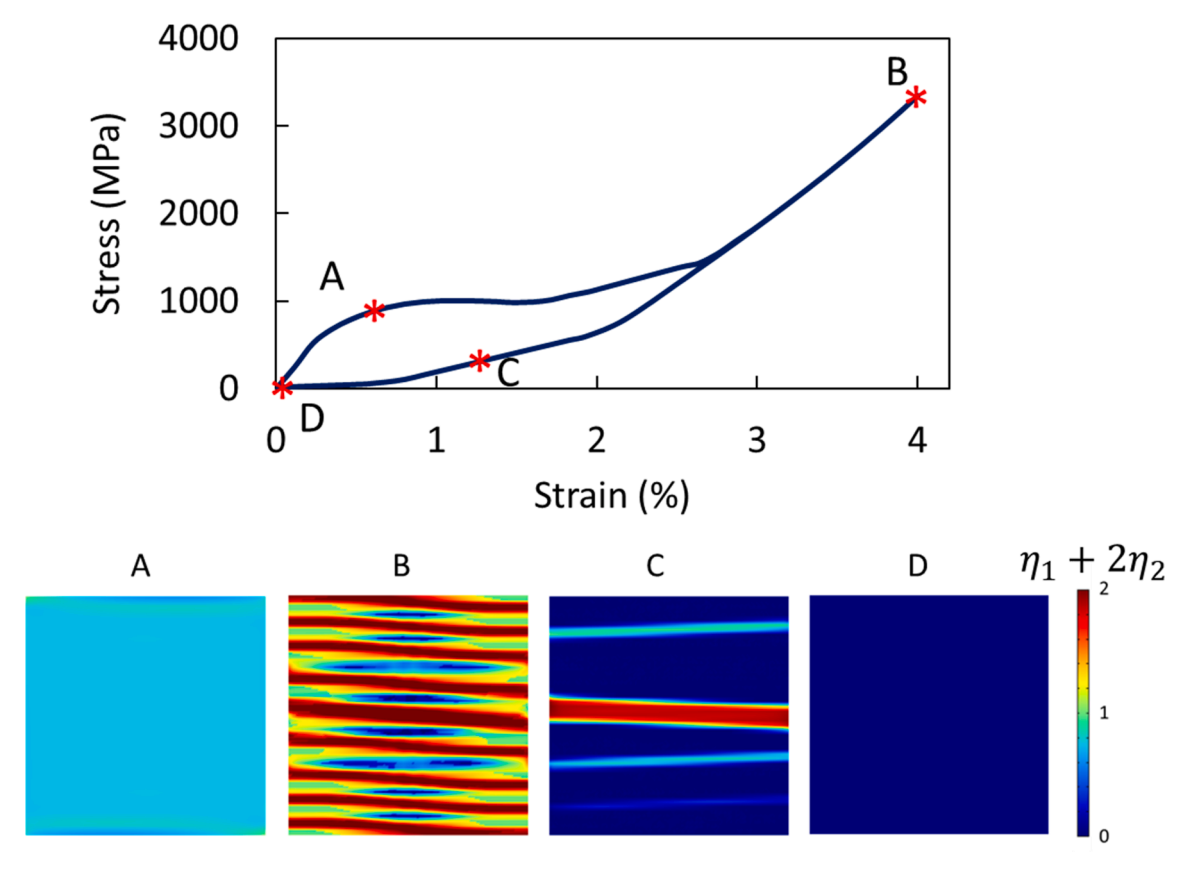


Fig. 5. Predicted stress-strain curve and microstructure for [001] orinted smaple by modified $F_{\rm ch}$.

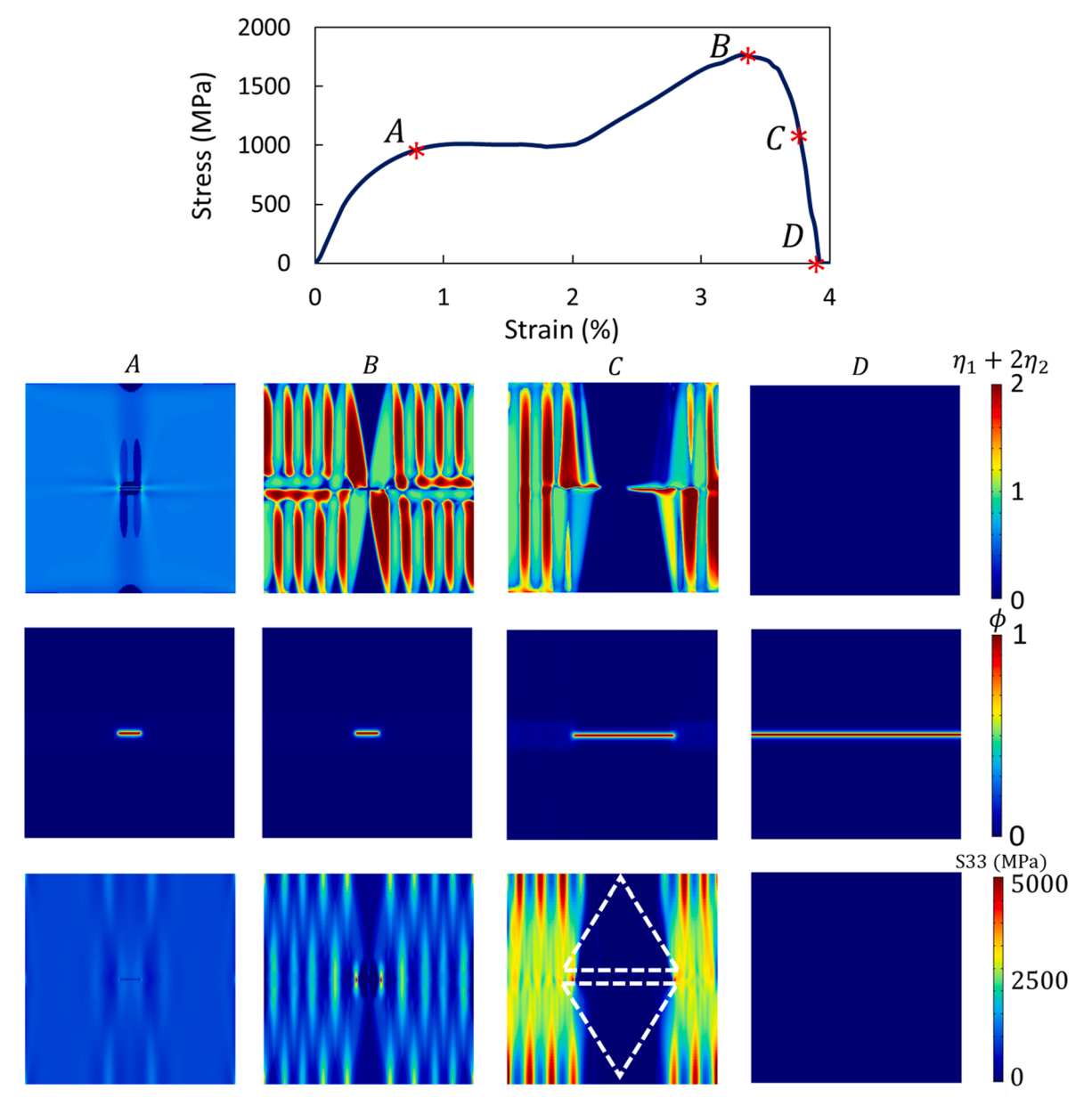


Fig. 6. Stress-strain curve, MPT, crack path, and stress map for [001] oriented sample under uniaxial tension in the z direction.

value of η_p to ensure that the modified double-well $F_{\rm ch}$ and its first derivative (shown in Fig. 4b) are well defined around $\eta_p=0$. Considering this modification, the Eq. (18) will change to:

$$\frac{\delta F_{\text{ch}}}{\delta \eta_p} = \Delta G \left(2a\eta_p - 3b\eta_p^2 + 4c\eta_p \sum_{p=1}^m \eta_p^2 + nd \left| \eta_p \right|^{n-1} \text{sign}(\eta_p) \right)$$
(37)

Since the proposed modification is for controlling the rate of OPs by adding an extra term of $d\sum_{p=1}^{m}\left|\eta_{p}\right|^{n}$, it can be easily applied to 2-4-6 form of F_{ch} as well.

To examine the modified $F_{\rm ch}$ in terms of microstructure and mechanical response prediction, by choosing n=1.1 and considering the same ΔG , we determine a,b,c, and d such that modified $F_{\rm ch}$ produces a double-well function close to the double-well $F_{\rm ch}$ seen in Fig. 2. The values of these parameters are presented in Table 3. Also, the same

domain and boundary conditions shown in Fig. 1 are considered. Fig. 4a shows the modified and unmodified double-well $F_{\rm ch}$. In both cases, $F_{\rm ch}$ has two minima, one at $\eta_p=0$ and one at $\eta_p=1$.

In Fig. 5, the modified $F_{\rm ch}$ predicts a plateau region in the stress-strain curve which is more realistic compared to the unmodified double-well. Additionally, it predicts the experimentally observed twin-martensite microstructures for zirconia-based ceramics [17].

Furthermore, the elastic modulus in the beginning of the stress-strain curve based on Fig. 5, is about 235 GPa, which is 5% less than the 247GPa. This shows that the modified PF model, has a low effect on the elastic modulus in the beginning of the stress-strain curve and yields a realistic stress-strain curve. In addition, this low error shows that n=1.1 is an acceptable choice. In the following section we use the modified PF model to study the interaction of fracture and MPT.

3.3. Interaction of MPT and fracture

The modified $F_{\rm ch}$ is used to study the interaction between MPT and fracture in a pre-cracked 3Y-STZ single crystal. Three different crystal orientations of $\theta=0^\circ$ ([001]), $+15^\circ$ ([$\bar{1}$ 04]), and 90° ([100]) are considered. The domain of Fig. 1 is considered with an initial center crack of 0.2µm (10% of the domain width) which is modeled with a Dirichlet boundary condition of $\phi=1$ imposed on the initial crack length. A monotonically increasing displacement rate of $u^*=2\times 10^{-3\frac{\mu m}{s}}$ is imposed on the top surface. Linear quadrilateral elements with a maximum size of 0.008µm, which is equal to 0.4k, is used in the sample. This element size is chosen based on the element size suggested by Miehe et al. [65]. In their work they suggested that the maximum size of the quadrilateral elements must be less than 50 percent of the k to ensure accuracy and convergence. Additionally, to reduce the computational demand of the model, only the elements within $\pm 0.2~\mu m$ of the horizontal centerline are given degree of freedom for the crack phase field.

Fig. 6 shows the obtained stress-strain curve, MPT, crack path, and stress map (S33 is shown which is the z component of stress tensor and is in the direction of applied displacement) for four different points on the stress-strain curve. As it is expected, since the stress concentration is high around the crack tips, the transformation starts from the crack tips and then spreads to the other regions of the sample, similar to experimental observations [66]. Also, according to Fig. 6, as the crack propagates, the reverse MPT (from monoclinic to tetragonal) occurs behind the crack tips (in the wake of the crack tips). This reverse MPT is in a good agreement with the experimental observation for crack propagation in the SE shape memory materials [67]. This reverse MPT occurs because in the SE regime, the reverse MPT occurs in the regions which experience unloading. This unloading is due to diminished load bearing capability resulting from separation of crack faces in the wake of the crack tips. This unloading process is clearly shown in the stress map in the third row of Fig. 6. The white triangles in the stress map indicate the regions behind the crack tips that unloading occurs at point *C* in Fig. 6.

In Fig. 6, before the start of the plateau region in the stress-strain curve (before point *A*), the sample is mostly in tetragonal phase. After this point, the phase transformation starts from the crack tips and then propagates to the rest of the sample. Based on Fig. 6, the ultimate strain is 4%. In the experimental study by Lai et al. [8], a maximum bending strain of 8% was reported for a coarse-grained micropillar specimen. Therefore, a model prediction of the maximum strain for a cracked single crystal experiencing uniaxial tension is expected to be less than the reported maximum bending strain. Furthermore, our model predicts the stress drop observed in the displacement-controlled loading experiments due to the crack propagation (between point *B* and *D*) which was not captured in [29,30] due to using the stress-controlled loading conditions.

Fig. 7 depicts both the average volume fraction of the monoclinic variants and half crack length versus applied displacement. This figure shows that MPT starts as soon as the load is applied, and the crack starts to propagate after the applied displacement reaches to $0.008\mu m$ (point a). In addition, after the crack length reaches to about $0.45\mu m$ (point c), the average volume fraction of the monoclinic variants starts to decrease and will become zero after the crack is fully developed. The average volume fraction of the monoclinic variants decreases due to the reverse MPT happening beyond the crack tips.

In Fig. 7, the crack advances at a low rate until its half-length grows to about $0.12\,\mu m$ (point b). The crack then grows at a very high rate until it propagates through the whole domain. This behavior is indicative of the rising R-curve behavior due to transformation toughening in yttria-stabilized zirconia ceramics [68–70] which is captured by our phase-field simulations.

In order to test the validity of microstructure prediction and crack path by the proposed phase-field model, we repeated the uniaxial tension simulation for $[\bar{1}04]$ oriented sample. Fig. 8 shows the obtained microstructure, crack path, and stress map (S33 component). The deformed shape of the domain is also provided in the fourth row. Fig. 8b depicts the experimental microstructure and crack path for a zirconia

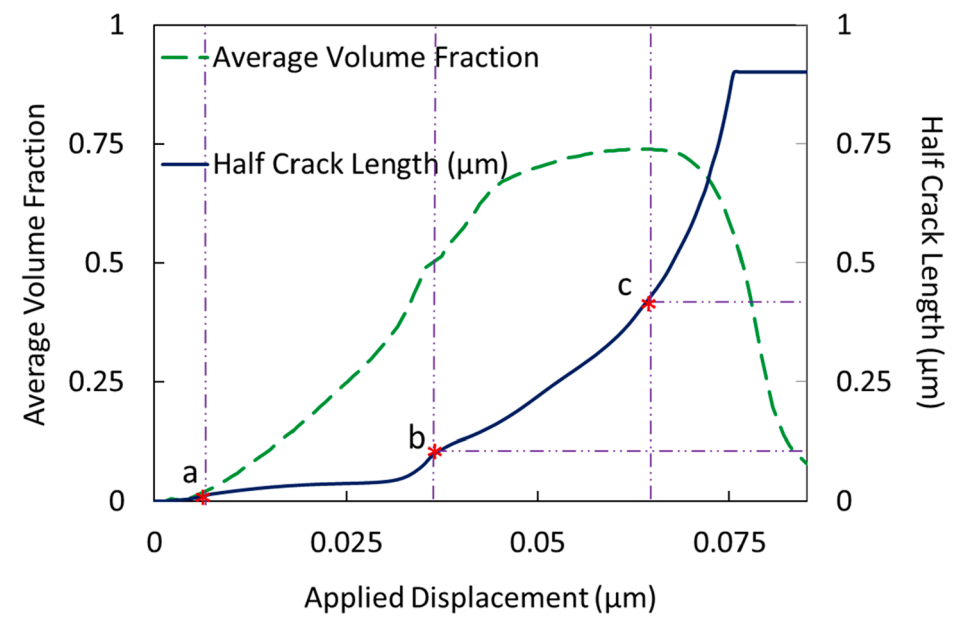


Fig. 7. The average volume fraction of the monoclinic variants vs. half crack length versus applied displacement for [001] oriented sample.

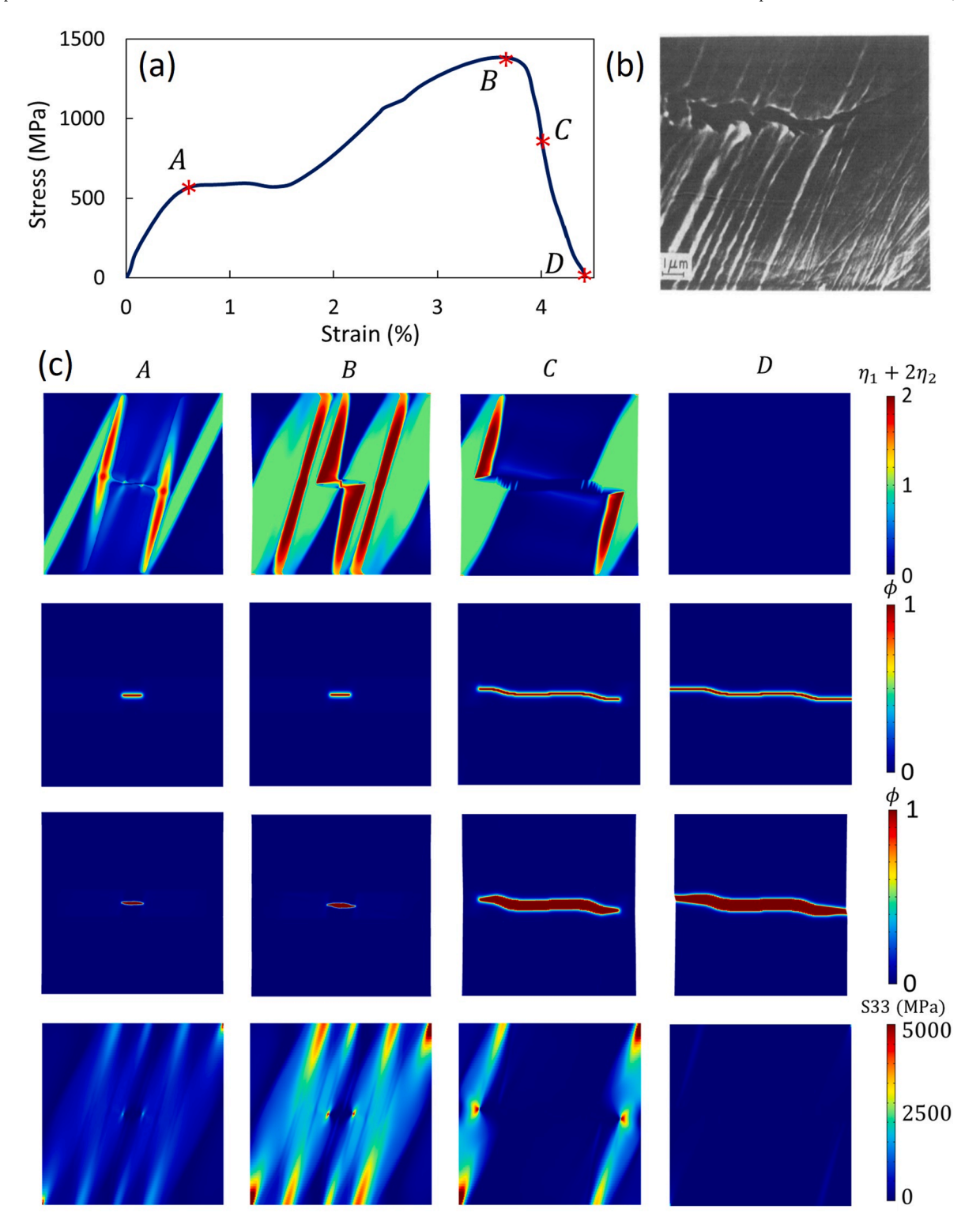


Fig. 8. Uniaxial tension of [104] oriented sample in z direction: a) Stress-strain curve from PF simulation, b) Experimentally observed MPT and crack deflection due to PT in a zirconia-based ceramic [9], and c) MPT (first row), crack path (second row: undeformed, and third row: deformed), and stress map (fourth row) from PF simulation.

based ceramic [9] with a similar crystal orientation with respect to crack direction. In this experiment, the material was in SE regime, and the reverse PT behind the crack tip and crack deflection due to PT were observed when crack propagated. As it can be seen in Fig. 8 our model accurately captures the reverse PT and crack deflection due to MPT similar to the experimental results. By comparing Fig. 6 and. Fig. 8a, it is evident that the crystal orientation affects the mechanical response,

direction (distribution pattern) of transformed regions, and crack path. The rotation of the stiffness tensor and the stress-free strain tensor lead to a different transformation stress (point A) and different fracture stress (σ_F) (point B) for different crystal orientations. The predicted transformation and fracture stresses are 1000 MPa and 1800 MPa for [001] and 600 MPa and 1400 MPa for [$\bar{1}$ 04] oriented sample. According to the zirconia-based coarse-grained micropillar bending test [8], a

transformation stress of about 1200 MPa and a fracture stress of about 2200 MPa were reported, therefore, we can conclude that our proposed modified model is able to quantitatively predict the mechanical behavior of SE zirconia and effectively captures the effect of grain orientation on predicting the mechanical response and microstructure.

Finally, the case of $\theta=90^\circ$ ([100]) was considered. The results are not presented here as neither phase transformation nor crack deflection occurred in this case. For this crystal orientation under the applied displacement boundary condition, a very small elongation occurs in the [001] direction, MPT is not considerable, and only a straight fracture path is observed. The mechanical response and crack path are an indication of a purely brittle material behavior. These predictions are consistent with the previously reported results by PFM [3] and MD [71] simulations, showing the importance of crystal orientation on the overall behavior of SMCs.

4. Conclusion

We presented a modified phase-field model for studying interactions of MPT and cracking in a superelastic 3 mol% yttria-stabilized tetragonal zirconia crystal. We identified the following shortcomings in previous PF studies coupling MPT and cracking:

- The interaction between SE behavior due to MPT and crack propagation at the microscale were not studied previously.
 Therefore, the reverse MPT due to crack propagation was not simulated previously.
- II. In many MPT models the elastic modulus is not recovered in the initial stages of the loading, and this is due to the high evolution rate of the order parameter(s) at the beginning of loading.
- III. In previously reported stress-strain curves, stress drop due to crack propagation was not captured, therefore, a conclusion about the strength of the material could not be made. This shortcoming is typically due to the use of stress-controlled boundary conditions, which were used in most previous models.

In this paper, we addressed these shortcomings, by modifying the chemical free energy and enabling displacement-controlled boundary conditions. The modification included adding an extra term to the 2-3-4 chemical free energy to accurately predict the mechanical response and reversible tetragonal to monoclinic transformation. This added term gives more control on the phase transformation rate (evolution of order parameters) and solves the problem of underestimating the elastic modulus observed in other phase-field models. The obtained results for transformation assisted deformation showed that the modified model is capable of predicting a realistic mechanical response, the experimentally observed microstructure, and the forward and reverse phase transformation in shape memory ceramics.

In addition, we applied the modified phase-field to study transformation-fracture interactions under displacement-controlled loading condition. We also studied the effect of different crystal orientation with respect to loading direction. The model can predict a realistic mechanical response and fracture strain, the experimentally observed microstructure and crack path due to phase transformation, the effect of grain orientation on both microstructure and mechanical response, and the reverse phase transformation due to crack propagation in superelastic shape memory ceramics. In addition, since we applied a displacement-controlled boundary condition, we were able to observe a final drop in the stress-strain curve due to crack propagation and establish a strength close to experimentally reported one for zirconiabased ceramics. Comparisons with experiments showed that the proposed modified model effectively captures accurate microstructures and crack deflection due to phase transformation and provides an admissible stress-strain curve. Such interactions between MPT and cracking are difficult to investigate by experiments which show advantage of phasefield modeling in the study of interactions of phase transformation and cracking.

CRediT authorship contribution statement

Amirreza Lotfolahpour: Conceptualization, Methodology, Software, Formal analysis, Writing – original draft. William Huber: Methodology, Formal analysis, Writing – review & editing. Mohsen Asle Zaeem: Supervision, Conceptualization, Methodology, Formal analysis, Writing – review & editing, Funding acquisition.

Declaration of Competing Interest

The authors declare that they have no known competing financial interests or personal relationships that could have appeared to influence the work reported in this paper.

Acknowledgement

This work was supported by the U.S. National Science Foundation, under Award number 2054274. The authors are grateful for the computer time allocation provided by the Extreme Science and Engineering Discovery Environment (XSEDE) to complete the simulations.

Data Availability

The datasets generated and/or analyzed in this study are available from the corresponding author on reasonable request.

References

- [1] K. Otsuka, C.M. Wayman, Shape memory materials, Cambridge university press,
- [2] M. Mamivand, M. Asle Zaeem, H. El Kadiri, A review on phase field modeling of martensitic phase transformation, Comput. Mater. Sci. 77 (2013) 304–311.
- [3] C. Cissé, M. Asle Zaeem, A phase-field model for non-isothermal phase transformation and plasticity in polycrystalline yttria-stabilized tetragonal zirconia, Acta Mater. 191 (2020) 111–123.
- [4] M. Simoes, E. Martínez-Pañeda, Phase field modelling of fracture and fatigue in Shape Memory Alloys, Comput. Methods Appl. Mech. Eng. 373 (2021), 113504.
- [5] E. Jebellat, M. Baniassadi, A. Moshki, K. Wang, M. Baghani, Numerical investigation of smart auxetic three-dimensional meta-structures based on shape memory polymers via topology optimization, J. Intell. Mater. Syst. Struct. 31 (15) (2020) 1838–1852.
- [6] N. Roudbarian, E. Jebellat, S. Famouri, M. Baniasadi, R. Hedayati, M. Baghani, Shape-memory polymer metamaterials based on triply periodic minimal surfaces, European Journal of Mechanics-A/Solids (2022), 104676.
- [7] C. Cissé, M. Asle Zaeem, Defect-induced asymmetrical mechanical behavior in shape memory zirconia: A phase-field investigation, J. Eur. Ceram. Soc. 42 (10) (2022) 4296–4310.
- [8] A. Lai, Z. Du, C.L. Gan, C.A. Schuh, Shape memory and superelastic ceramics at small scales, Science 341 (6153) (2013) 1505–1508.
- [9] A.G. Evans, R. Cannon, Toughening of brittle solids by martensitic transformations, Acta Metall.; (United States) 34 (5) (1986).
- [10] T.W. Coyle, W.S. Coblenz, B.A. Bender, Transformation Toughening in Large-Grain-Size CeO2-Doped ZrO2 Polycrystals, J. Am. Ceram. Soc. 71 (2) (1988) C-88-C-92.
- [11] M. Ambati, T. Gerasimov, L. De Lorenzis, A review on phase-field models of brittle fracture and a new fast hybrid formulation, Comput. Mech. 55 (2) (2015) 383–405.
- [12] M.J. Borden, C.V. Verhoosel, M.A. Scott, T.J. Hughes, C.M. Landis, A phase-field description of dynamic brittle fracture, Comput. Methods Appl. Mech. Eng. 217 (2012) 77–95.
- [13] A. Lotfolahpour, M. Asle Zaeem, Effects of cleavage plane and material strength on fracture of polycrystalline brittle materials: A phase-field modeling study, Comput. Mater. Sci. 197 (2021), 110642.
- [14] S. Rezaei, A. Harandi, T. Brepols, S. Reese, An anisotropic cohesive fracture model: advantages and limitations of length-scale insensitive phase-field damage models, Eng. Fract. Mech. 108177 (2022).
- [15] M. Ambati, T. Gerasimov, L. De Lorenzis, Phase-field modeling of ductile fracture, Comput. Mech. 55 (5) (2015) 1017–1040.
- [16] M.J. Borden, T.J. Hughes, C.M. Landis, A. Anvari, I.J. Lee, A phase-field formulation for fracture in ductile materials: Finite deformation balance law derivation, plastic degradation, and stress triaxiality effects, Comput. Methods Appl. Mech. Eng. 312 (2016) 130–166.
- [17] R.H. Hannink, P.M. Kelly, B.C. Muddle, Transformation toughening in zirconiacontaining ceramics, J. Am. Ceram. Soc. 83 (3) (2000) 461–487.
- [18] W. Gao, X. Yi, G. Song, Z. Wang, X. Meng, Zr50Cu25Ni7. 5Co17. 5 high-temperature shape memory alloy with excellent thermal stability and large

- recovery strain, and the associated microstructural deformation mechanism, Mater. Des. 196 (2020) 109108.
- [19] M. Mamivand, M. Asle Zaeem, H. El Kadiri, L.-Q. Chen, Phase field modeling of the tetragonal-to-monoclinic phase transformation in zirconia, Acta Mater. 61 (14) (2013) 5223–5235.
- [20] M. Mamivand, M. Asle Zaeem, H. El Kadiri, Shape memory effect and pseudoelasticity behavior in tetragonal zirconia polycrystals: A phase field study, Int. J. Plast. 60 (2014) 71–86.
- [21] Y. Sun, J. Luo, J. Zhu, Ferroelastic toughening of single crystalline yttria-stabilized t'zirconia: A phase field study, Eng. Fract. Mech. 233 (2020), 107077.
- [22] B. Xu, G. Kang, C. Yu, Q. Kan, Phase field simulation on the grain size dependent super-elasticity and shape memory effect of nanocrystalline NiTi shape memory alloys, Int. J. Eng. Sci. 156 (2020), 103373.
- [23] B. Xu, G. Kang, Phase field simulation on the super-elasticity, elastocaloric and shape memory effect of geometrically graded nano-polycrystalline NiTi shape memory alloys, Int. J. Mech. Sci. 201 (2021), 106462.
- [24] Y. Zhong, T. Zhu, Phase-field modeling of martensitic microstructure in NiTi shape memory alloys, Acta Mater. 75 (2014) 337–347.
- [25] H.M. Paranjape, S. Manchiraju, P.M. Anderson, A phase field–Finite element approach to model the interaction between phase transformations and plasticity in shape memory alloys, Int. J. Plast. 80 (2016) 1–18.
- [26] S. Xi, Y. Su, Phase field study of the microstructural dynamic evolution and mechanical response of NiTi shape memory alloy under mechanical loading, Materials 14 (1) (2021) 183.
- [27] T. Zhao, J. Zhu, J. Luo, Study of crack propagation behavior in single crystalline tetragonal zirconia with the phase field method, Eng. Fract. Mech. 159 (2016) 155-173
- [28] J. Zhu, J. Luo, Study of transformation induced intergranular microcracking in tetragonal zirconia polycrystals with the phase field method, Mater. Sci. Eng., A 701 (2017) 69–84.
- [29] E. Moshkelgosha, M. Mamivand, Phase field modeling of crack propagation in shape memory ceramics-Application to zirconia, Comput. Mater. Sci. 174 (2020), 109509
- [30] E. Moshkelgosha, M. Mamivand, Concurrent modeling of martensitic transformation and crack growth in polycrystalline shape memory ceramics, Eng. Fract. Mech. 241 (2021), 107403.
- [31] E. Moshkelgosha, M. Mamivand, Three-dimensional phase field modeling of fracture in shape memory ceramics, Int. J. Mech. Sci. 204 (2021), 106550.
- [32] K. Noguchi, M. Fujita, T. Masaki, M. Mizushina, Tensile strength of yttria-stabilized tetragonal zirconia polycrystals, J. Am. Ceram. Soc. 72 (7) (1989) 1305–1307.
- [33] J. Kondoh, H. Shiota, K. Kawachi, T. Nakatani, Yttria concentration dependence of tensile strength in yttria-stabilized zirconia, J. Alloy. Compd. 365 (1–2) (2004) 253–258
- [34] K. Noguchi, Y. Matsuda, M. Oishi, T. Masaki, S. Nakayama, M. Mizushina, Strength analysis of yttria-stabilized tetragonal zirconia polycrystals, J. Am. Ceram. Soc. 73 (9) (1990) 2667–2676.
- [35] M. Oishi, Y. Matsuda, K. Noguchi, T. Masaki, Evaluation of Tensile Strength and Fracture Toughness of Yttria-Stabilized Zirconia Polycrystals with Fracture Surface Analysis, J. Am. Ceram. Soc. 78 (5) (1995) 1212–1216.
- [36] K. Gall, N. Yang, H. Sehitoglu, Y.I. Chumlyakov, Fracture of precipitated NiTi shape memory alloys, Int. J. Fract. 109 (2) (2001) 189–207.
- [37] L. Krone, E. Schüller, M. Bram, O. Hamed, H.-P. Buchkremer, D. Stöver, Mechanical behaviour of NiTi parts prepared by powder metallurgical methods, Mater. Sci. Eng., A 378 (1–2) (2004) 185–190.
- [38] S. Gollerthan, M. Young, A. Baruj, J. Frenzel, W.W. Schmahl, G. Eggeler, Fracture mechanics and microstructure in NiTi shape memory alloys, Acta Mater. 57 (4) (2009) 1015–1025.
- [39] A. Creuziger, L. Bartol, K. Gall, W. Crone, Fracture in single crystal NiTi, J. Mech. Phys. Solids 56 (9) (2008) 2896–2905.
- [40] A. Dehghani, F. Aslani, Crack recovery and re-centring performance of cementitious composites with pseudoelastic shape memory alloy fibres, Constr. Build. Mater. 298 (2021), 123888.
- [41] Z. Chen, H.L. Schreyer, A numerical solution scheme for softening problems involving total strain control, Comput. Struct. 37 (6) (1990) 1043–1050.
- [42] Y. Sun, J. Luo, J. Zhu, K. Zhou, A non-isothermal phase field study of the shape memory effect and pseudoelasticity of polycrystalline shape memory alloys, Comput. Mater. Sci. 167 (2019) 65–76.
- [43] Y. Wen, Y. Wang, L.-Q. Chen, Effect of elastic interaction on the formation of a complex multi-domain microstructural pattern during a coherent hexagonal to orthorhombic transformation, Acta Mater. 47 (17) (1999) 4375–4386.
- [44] Y. Zhang, X. Jin, T. Hsu, Thermodynamic calculation of Ms in ZrO2–CeO2–Y2O3 system, J. Eur. Ceram. Soc. 23 (5) (2003) 685–690.
- [45] B. Bourdin, G.A. Francfort, J.-J. Marigo, Numerical experiments in revisited brittle fracture, J. Mech. Phys. Solids 48 (4) (2000) 797–826.

- [46] C. Kuhn, A. Schlüter, R. Müller, On degradation functions in phase field fracture models, Comput. Mater. Sci. 108 (2015) 374–384.
- [47] N. Nguyen-Thanh, W. Li, J. Huang, K. Zhou, Adaptive higher-order phase-field modeling of anisotropic brittle fracture in 3D polycrystalline materials, Comput. Methods Appl. Mech. Eng. 372 (2020), 113434.
- [48] C. Miehe, M. Hofacker, F. Welschinger, A phase field model for rate-independent crack propagation: Robust algorithmic implementation based on operator splits, Comput. Methods Appl. Mech. Eng. 199 (45–48) (2010) 2765–2778.
- [49] L.D. Landau, Collected papers of LD Landau, Pergamon, 1965.
- [50] S.M. Allen, J.W. Cahn, A microscopic theory for antiphase boundary motion and its application to antiphase domain coarsening, Acta Metall. 27 (6) (1979) 1085–1095.
- [51] M. Hofacker, C. Miehe, Continuum phase field modeling of dynamic fracture: variational principles and staggered FE implementation, Int. J. Fract. 178 (1) (2012) 113–129.
- [52] J. Chevalier, L. Gremillard, A.V. Virkar, D.R. Clarke, The tetragonal-monoclinic transformation in zirconia: lessons learned and future trends, J. Am. Ceram. Soc. 92 (9) (2009) 1901–1920.
- [53] H. Scott, Phase relationships in the zirconia-yttria system, J. Mater. Sci. 10 (9) (1975) 1527–1535.
- [54] E.H. Kisi, C.J. Howard, Elastic constants of tetragonal zirconia measured by a new powder diffraction technique, J. Am. Ceram. Soc. 81 (6) (1998) 1682–1684.
- [55] X.-S. Zhao, S.-L. Shang, Z.-K. Liu, J.-Y. Shen, Elastic properties of cubic, tetragonal and monoclinic ZrO2 from first-principles calculations, J. Nucl. Mater. 415 (1) (2011) 13–17.
- [56] M. Asle Zaeem, H. El Kadiri, S.D. Mesarovic, M.F. Horstemeyer, P.T. Wang, Effect of the compositional strain on the diffusive interface thickness and on the phase transformation in a phase-field model for binary alloys, Journal of phase equilibria and diffusion 32 (4) (2011) 302–308.
- [57] A. Emdadi, W.G. Fahrenholtz, G.E. Hilmas, M. Asle Zaeem, A modified phase-field model for quantitative simulation of crack propagation in single-phase and multiphase materials, Eng. Fract. Mech. 200 (2018) 339–354.
- [58] A. Emdadi, M. Asle Zaeem, Phase-field modeling of crack propagation in polycrystalline materials, Comput. Mater. Sci. 186 (2021), 110057.
- [59] H. Amor, J.-J. Marigo, C. Maurini, Regularized formulation of the variational brittle fracture with unilateral contact: Numerical experiments, J. Mech. Phys. Solids 57 (8) (2009) 1209–1229.
- [60] A. Loganathan, A.S. Gandhi, Effect of phase transformations on the fracture toughness of t' yttria stabilized zirconia, Mater. Sci. Eng., A 556 (2012) 927–935.
- [61] S.E. Esfahani, I. Ghamarian, V.I. Levitas, P.C. Collins, Microscale phase field modeling of the martensitic transformation during cyclic loading of NiTi single crystal, Int. J. Solids Struct. 146 (2018) 80–96.
- [62] X. Li, Y. Su, A phase-field study of the martensitic detwinning in NiTi shape memory alloys under tension or compression, Acta Mech. 231 (4) (2020) 1539–1557.
- [63] B. Xu, C. Yu, G. Kang, Phase field study on the microscopic mechanism of grain size dependent cyclic degradation of super-elasticity and shape memory effect in nanopolycrystalline NiTi alloys, Int. J. Plast. 145 (2021), 103075.
- [64] J. Zhu, J. Luo, Y. Sun, Phase field study of the grain size and temperature dependent mechanical responses of tetragonal zirconia polycrystals: A discussion of tension-compression asymmetry, Comput. Mater. Sci. 172 (2020), 109326.
- [65] C. Miehe, F. Welschinger, M. Hofacker, Thermodynamically consistent phase-field models of fracture: Variational principles and multi-field FE implementations, Int. J. Numer. Meth. Eng. 83 (10) (2010) 1273–1311.
- [66] S. Deville, H. El Attaoui, J. Chevalier, Atomic force microscopy of transformation toughening in ceria-stabilized zirconia, J. Eur. Ceram. Soc. 25 (13) (2005) 3089–3096.
- [67] S. Robertson, A. Mehta, A. Pelton, R. Ritchie, Evolution of crack-tip transformation zones in superelastic Nitinol subjected to in situ fatigue: A fracture mechanics and synchrotron X-ray microdiffraction analysis, Acta Mater. 55 (18) (2007) 6198–6207.
- [68] D. Casellas, J. Alcala, L. Llanes, M. Anglada, Fracture variability and R-curve behavior in yttria-stabilized zirconia ceramics, J. Mater. Sci. 36 (12) (2001) 3011–3025.
- [69] S.Y. Liu, I.W. Chen, Fatigue of Yttria-Stabilized Zirconia: II, Crack Propagation, Fatigue Striations, and Short-Crack Behavior, J. Am. Ceram. Soc. 74 (6) (1991) 1206–1216.
- [70] J. Chevalier, C. Olagnon, G. Fantozzi, Crack propagation and fatigue in zirconia-based composites, Compos. A Appl. Sci. Manuf. 30 (4) (1999) 525–530.
- [71] N. Zhang, M. Asle Zaeem, Competing mechanisms between dislocation and phase transformation in plastic deformation of single crystalline yttria-stabilized tetragonal zirconia nanopillars, Acta Mater. 120 (2016) 337–347.